Briand *et al. Earth, Planets and Space* (2022) 74:41
https://doi.org/10.1186/s40623-022-01598-2

Earth, Planets and Space

FULL PAPER Open Access

Role of hard X-ray emission in ionospheric D-layer disturbances during solar flares

Carine Briand[1*], Mark Clilverd[2], Srivani Inturi[1] and Baptiste Cecconi[1]

Abstract

Any disturbance of the ionosphere may affect operational activities based on HF communication. The electron density is a critical parameter that controls levels of HF-signal absorption. A significant part of the HF absorption takes place in the D-layer. The increase of X radiations during solar flares generates noticeable perturbations of the electron density of the D-layer. However, the ionosphere reacts with some delay to the solar forcing. Several studies have addressed this question of ionospheric sluggishness from the time delay between VLF narrow-band transmissions and soft X-ray emissions during solar flares. Our study initially considers the interpretation of the VLF amplitude time profile. In particular, we show that the maximum of X-ray emission can be associated with a reversal in the VLF amplitude variation with time, i.e. exhibiting a peak or a trough. Then, building on this insight, we perform estimates of the time delay between VLF and soft X-rays during 67 events between 2017 and 2021, thus including the major flares of 2017. We show that the time delay can become negative for flares above X2, proving that soft X-rays are not the initial source of ionization in the case of major flares. From a careful analysis of RHESSI data for some events of September 2017, we demonstrate that radiation above 40 keV (i.e. hard X-rays) is an important forcing source of the ionosphere. This is of crucial interest in the frame of space weather forecasting since the hard X-rays are produced several minutes before the peak of soft X-rays.

Keywords: VLF, Ionosphere, Solar flares, X-ray

Graphical Abstract

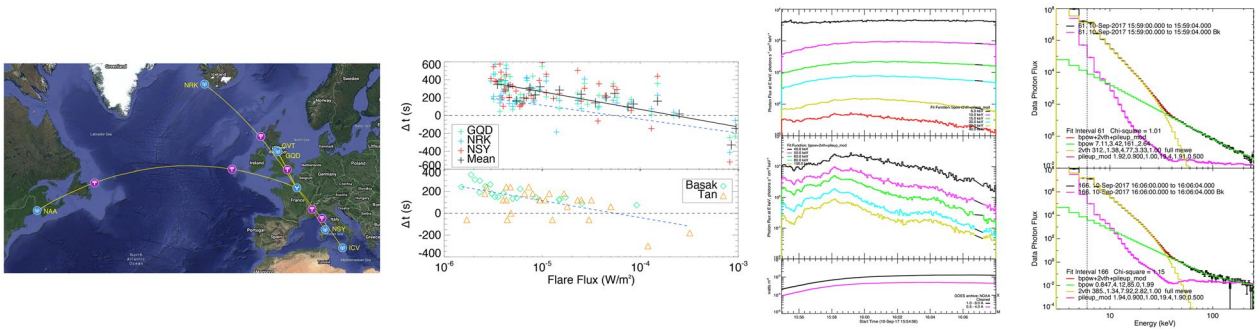

Introduction

High-frequency (HF, 3–30 MHz) emissions are crucial for many communication operators, like aviation, over the horizon radars, shipping, broadcasting or security

*Correspondence: carine.briand@obspm.fr
[1] LESIA, Observatoire de Paris-PSL, CNRS, Sorbonne Université, Université Paris Cité, Paris, France
Full list of author information is available at the end of the article

services. The long distance communication HF signal relies on reflection by the ionosphere. Thus, any disturbance of the ionosphere may affect operational activities based on HF communication. The electron density is a critical parameter that controls levels of HF-signal absorption (also called short-wave fadeout when it concerns the 3–30 MHz range) and signal phase-shift (Doppler flash) (Dellinger 1935; Ellison 1950; Siskind et al. 2017; Chakraborty et al. 2018; Tao et al. 2020, and references therein). The D-layer is the lowest layer of the Earth ionosphere ($\sim$ 60–90 km). HF signals pass through this layer to reach altitudes where they reflected back to the ground (crossing the D-layer a second time). The largest part of the HF absorption takes place in the D-layer. Thus an accurate understanding of electron density variations in space and time are necessary.

The D-region electron density depends on several parameters, from a complicated chemistry involving many neutral species (Verronen et al. 2016), ionization from particle precipitation from the magnetosphere and solar energetic radiation. In the following, we concentrate only this last parameter. During daytime, the solar UV and EUV radiation, in particular Lyman-α ($\lambda = 121.6$ nm), are the main source of ionization of the ionosphere. During nighttime, the L_α radiation is drastically reduced to the diffusion on the hydrogen geocorona and cosmic rays become the main source of ionization. The D-layer is thus strongly diminished at night. Other transient phenomena influence the ionization of the D-layer: solar flares, by their increase X-radiation (Deshpande et al. 1972; McRae and Thomson 2004), Transient luminous events (TLE, like sprites, elves of TGF) associated with thunderstorm regions (Haldoupis et al. 2004; NaitAmor et al. 2010; Haldoupis et al. 2012), and meteorites (De et al. 2011).

The D-layer covers an altitude range both too high for balloons and too low for satellites. Only rare and short-during rocket explorations have provided in situ measurements of the plasma parameters (for example Rose et al. 1972; Hall 1973). An efficient way to *remotely* diagnose the electron density of the D-layer consists of measuring the time evolution of VLF/LF waves (3–300 kHz) that propagate in the waveguide formed by the Earth and the ionosphere. For short VLF paths (typically below 2200 km), the received signal is the sum of a ground wave, i.e. the signal propagating directly to the receiver, and a single sky-wave, i.e. a wave bounced back to the Earth from the D-layer. This indirect method of monitoring the D-region has proven to be robust since the 1950s. In particular, it has been widely used to study the response of the D-layer to the X-ray insulation during solar flares.

Solar flares are eruptive phenomena taking place in the solar chromosphere and corona. They are characterized by a huge increase of the X-radiation and the emission of very energetic electrons in the interplanetary medium that can reach the Earth in a few hours. Our study focuses on the impacts of the X-ray on the D-layer. During flares, X-ray fluxes (0.1–10 nm) increase by several orders of magnitude within a few minutes and decays within several tens of minutes. This radiation is energetic enough to reach the deepest layers of the Earth atmosphere. It can cause significant ionization increases either through a direct ionization of the molecular species, in particular nitric oxide NO, or through the generation of secondary electrons. The reflected VLF signal amplitude and phase are affected as a result of the change of the D-layer conductivity induced by the electron density growth.

The electron loss processes (attachment, recombination) delay the ionosphere response to a change in the ionization. It is termed as sluggishness of the ionosphere or relaxation time Δt. Resolving the continuity equation and assuming an electron sink term as αN_e^2, with α the recombination rate and N_e the electron density, Appleton (1953) showed that Δt can be expressed as:

$$\Delta t = \left(\frac{1}{2\alpha N_e}\right). \tag{1}$$

Estimation of Δt is thus an efficient and easy way to determine the electron density variation and/or the effective recombination factor. Recently, Chakraborty et al. (2021) provided a new definition of time delay, based on solar irradiance and ionospheric response through HF absorption. We however, conserve the original definition as it provides information on the electron density at the maximum of ionization. Ellison (1950, 1953) noted that the maximum of "Sudden Enhancements of Atmospherics" (S.E.A) occurred several minutes ($\approx$ 6 min in their records) after the maximum flux of solar flares, as observed in Hα (see also, Křivský 1962). Owing to the development of rocket measurements, the contribution of the X-ray domain to D-region ionization was identified (Deshpande et al. 1972). As a result, Zigman et al. (2007) reconsidered the time delay between the soft X-ray maximum and the VLF peak time in order to determine the electron-density time variation during flare development. Basak and Chakrabarti (2013), following the same definition of Δt, showed that the time delay decreases with increasing flare flux (see also Tan et al. 2014; Palit et al. 2015). This trend is in agreement with the fact that the recombination factor increases as the reflection layer of the VLF wave decreases in altitude, due to the increase of collisions with neutrals. In this study, we follow the same procedure but take the opportunity of the September

2017 flares to check if the Δt trend is still valid for very powerful X-flares. We thus show that for such strong flares, hard X-rays plays a significant role, i.e. not only soft X-rays as considered in most of studies.

The paper is organized as follows: "Instrumentation and data reduction" section describes the experimental setup and details the event selection and data analysis procedures. "Analysis" section presents the analysis of the data, with a specific focus on the role of hard X-rays. "Conclusion" section provides the concluding remarks.

Table 1 Characteristics of the followed transmitters, ordered by frequency increase

Station	Freq. (kHz)	Distance (km)	Angle (°)	SR location
GQD	19.58	777	330.9	51N01E
ICV	20.28	1057	146.1	45N06E
GVT	22.10	746	331.9	51N00E
NAA	24.00	5132	265.0	51N15W
NRK	37.50	2234	318.2	56N07W
NSY	45.90	1632	142.7	43N08E

The first two columns give the station name and the transmission frequency, the third column indicates the distance to Meudon along a Great Circle Path, the fourth column gives the azimuth angle of the transmitter to Meudon. The fifth column indicates the location of the sub-reflection (SR) area

Instrumentation and data reduction

VLF antenna characteristics

VLF amplitudes are recorded from a SUPERSID instrument Scherrer et al. (2008) located at the Meudon site of the Paris Observatory, France (02°13′40″ East, 48°48′36″ North, Altitude: 162 m). The magnetic-loop antenna is 2m in size. A spectrum is computed between 10 and 70 kHz, integrating the signal over 1 s. The maximum amplitude is conserved for six frequencies (100-Hz bandwidth), corresponding to six ground-based transmitters, with a period of 5 s. Only amplitude is measured. Four stations have been continuously recorded since January 1st, 2017. The two last channels were used for tests and finally tuned to selected transmitters at the end of 2017. Table 1 displays the characteristics of the transmitters regularly followed. All paths (except NAA-Meudon) are short enough in distance to Meudon to propagate through a single-hop reflection on the ionosphere (as checked from the single minimum observed during night/day transition). Three transmitters are used in particular for the present study: GQD, NRK, and NSY. Three reasons for this transmitter's choice. First, as can be appreciated from Fig. 1, they are almost aligned, which enables to optimize the antenna orientation. Then, they have been continuously followed since January 1st, 2017 and finally they are oriented almost North–South, which

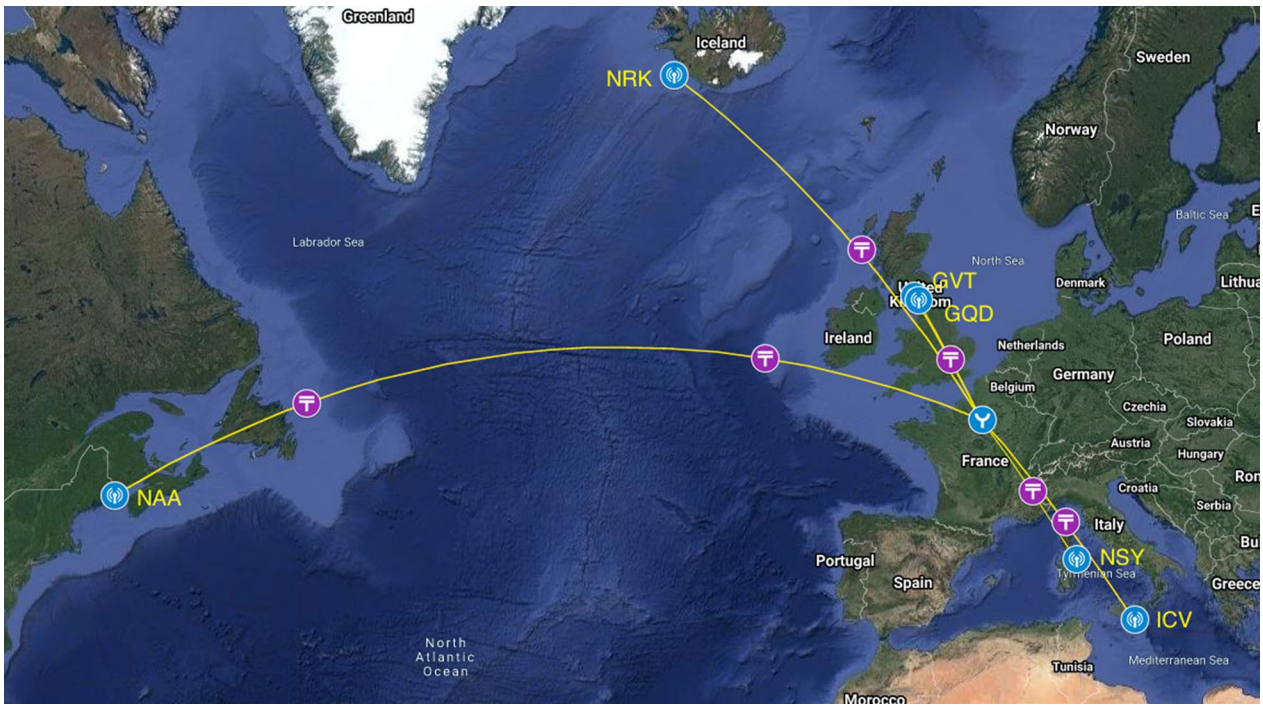

Fig. 1 Great Circle Path (GCP) between the VLF/LF stations used in the analysis and Meudon (France). Violet points indicate the sub-reflection area on the ionosphere. Blue circles indicate the transmitter location. Note that NRK, GVT (Skelton, Cumbria), GQD (Anthorn), ICV and NSY are almost aligned. The antenna is orientated to optimize their reception

limits the day–night terminator effects (Clilverd et al. 1999). Their sub-reflection areas cover a rather large latitudinal extension, from 43° to 56°.

The antenna is located in a historical castle, well isolated from electromagnetic contamination. This EM-clean environment limits the noise level to below 0.3dB at all frequencies, as determined when the transmitters are off. We have empirically estimated that flares above C3.0 (i.e. 3.10^{-6} W/m^2) are reliably detected. A Savitzky–Golay filter is however also applied to smooth the VLF data to increase the accuracy of the analysis.

The time profiles of the VLF measurements will be compared to those of GOES, in particular the soft X-rays (hereafter SXR) XL channel ($\lambda = 0.1-0.8$ nm), and hard X-rays (hereafter HXR) from RHESSI (Smith 2002; Lin 2002). The analysis is also supplemented by RHESSI spectra. RHESSI instrument is particularly interesting for its broad spectral coverage at high spectral resolution and continuous observations during sunlight phase of the orbit. The data were calibrated following the standard procedure of the RHESSI-GUI package and modelized following the Ospex package.

Flare events selection

Only flares above C3.0 class are considered for analysis, in accordance with the antenna detection limit. We also restrict to those flares with a solar zenith angle at the ionospheric reflection-point above 88° to keep only events occurring during daytime and remove those too close from to day–night transition period. As a result, 70 flares remained since 2017: 43 C-class, 20 M-class and 7 X-class. However, due to temporary shut-down of the transmitter or very unclear signal, the number of events studied from each transmitter varies. We finally analysed 53 events from GQD and NRK and 47 from NSY. The selected flare characteristics are listed in Table 2.

All except one of the X-class flares occurred between September 5 and September 10, 2017. During this period, an active region, NOAA 12673, was located on the Western side of the solar surface. It produced the strongest flares since 2005, an X9.3 on September 6 followed by an X8.2 flare on September 10. Those events induced strong space weather effects on GNSS and HF propagation (Yasyukevich et al. 2018; Redmon et al. 2018), and noticeable disturbances of the ionosphere and thermosphere (see for example Li et al. (2018); Bagiya et al. (2018); Qian et al. (2019)).

Time delay computation

Following former works (Zigman et al. 2007; Basak and Chakrabarti 2013; Tan et al. 2014; Palit et al. 2015), we define Δt as the difference between the time of the SXR maximum (T_{SXR}) and the time of the D-layer ionization-maximum (T_{VLF}):

$$\Delta t = T_{\mathrm{VLF}} - T_{\mathrm{SXR}}. \tag{2}$$

When the SXR emission peak occurs before the maximum of the VLF signal (T_{VLF}), Δt is positive. With the assumption that the maximum of ionization occurs when the VLF amplitude reaches its extrema value, Δt can lead to an estimate of the effective recombination rate, knowing the electron density (Eq. 1). The determination of T_{VLF} deserves a short discussion since it can correspond either to a maximum or a *minimum* perturbation amplitude.

Figure 2 displays the VLF time profile for several flares of increasing strength and the three transmitters (NRK on the top row, GQS in the middle row and NSY on the bottom row). Quiet time reference height is highest at highest latitudes. Also the lowest altitude a flare would reach would be lower at lower latitudes. And this is indicated in the panels.

Irrespective of the flare strength, VLF profiles from GQD always display an amplitude increase during the flare rise phase. A similar behaviour is observed from NRK, except for the very strong X9.3 flare when a sudden drop follows the first increase. However, the amplitude from NSY only displays an increase up to M6 flare levels, but for stronger flares a decrease is observed after an initial increase. Rozhnoi et al. (2019) presented a similar time profile for GQD-Birr path, i.e. UK–Ireland path (their Fig. 3). To understand which part of the VLF behaviour corresponds to the maximum of ionization (flare maximum), we need to compute the interference pattern for each path.

The VLF amplitude results from the interference of a ground and a sky wave, i.e. a wave propagating on the ground following the curvature of the Earth and a wave reflected in the ionosphere. The cosine of the path difference ϵ between the waves gives the signal amplitude modulation. For the fundamental mode (as can be expected from the short distance between the selected transmitters and receiver), the path difference is given by (Delcourt 2003):

$$\epsilon = \frac{2\sqrt{2R[R+h]\left[1-\cos\left(\frac{d_s}{2R}\right)\right]+h^2}-d_s}{\lambda}, \tag{3}$$

with R the Earth radius, h the effective reflection-height, d_s the distance transmitter–receiver along a Great Circle Path (GCP) and λ the wavelength of the emitted signal. The term $\cos(2\pi\epsilon)$ modulates the signal amplitude. As an example, Fig. 3 presents this modulation function vs. the reflection height, for the three paths (NRK-Meudon,

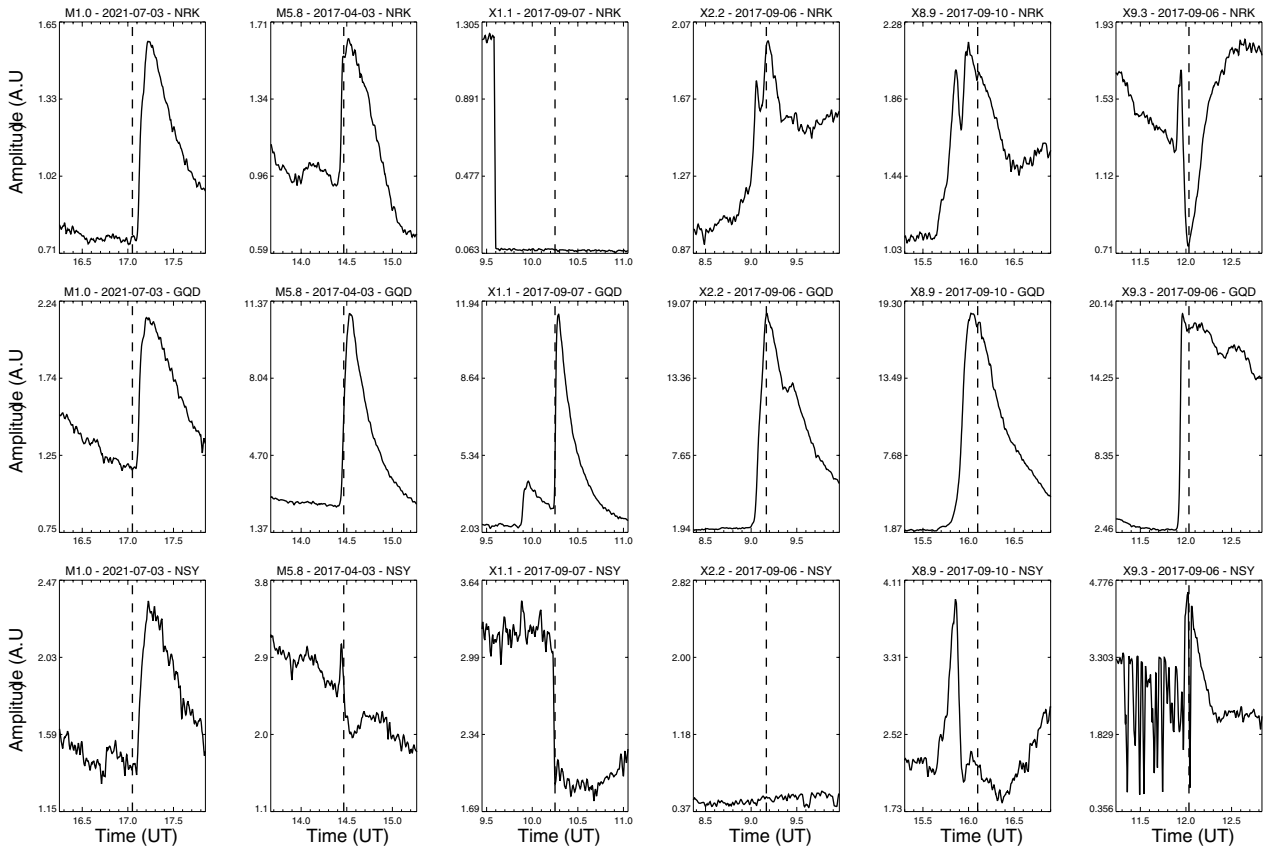

Fig. 2 Time profiles for several flares of increasing strength (column) and GQD, NRK and NSY (from top to bottom row). Vertical dashed lines indicate the flare peak time (as given by the GOES daily reports). Amplitudes are given in arbitrary units. NRK was off-air for the X1.1 flare, while NSY was off-air during the X2.2 and X9.3

GQD-Meudon, NSY-Meudon). During X-class flares, the reflection height decreases by 10 to 15 km (Fig. 9 of Thomson et al. 2005). For illustration purpose, let us consider a lowering of 12 km. This range of altitude, indicated by vertical dashed lines, and the arrow indicates the evolution of the cosine during the rise phase of the flare. During quiet periods, GQD emission reflects typically around 72±3 km (Grubor et al. 2008; Kolarski and Grubor 2015). The lowering of the reflection height during the flare corresponds to an increase of the cosine, thus an increase of the amplitude. To explain the profiles from NRK (see discussion above), the quiet reflection height must stand around 81 km, which is compatible with a sub-reflective point located at high latitude (large solar zenith angle): quiet time daytime reference height is higher at higher latitudes (Thomson et al. 2017). Also the lowest altitude a flare would influence would be lower at lower latitudes, consistent with the reduction in altitude of the left-hand vertical dashed line. During the rising phase of the flare, the cosine first increases then decreases if the height decrease is large enough (strong flare). For NSY, the decreases observed for rather weak flares lead us to consider a reflection height during quiet period around 71 km, which is also compatible with a sub-reflective point with small solar zenith angle. For a height lowering above 4 km (i.e. moderate flares), the cosine already decreases.

This simple analysis qualitatively explains the main features of observed amplitude. It also shows that the characteristic to consider for the computation of the time delay is either a maximum or a minimum not necessarily the largest or the smallest amplitude, but a reversal of amplitude change, i.e. a peak or a trough as the flux starts to decrease. It also shows that this characteristic can change with flare strength. Finally, since the interference pattern depends on the transmitter–receiver path, it must be computed for each situation. More complete computations (including all the modes) should indicate more accurately the height range to be considered: the values given above are just indicative. A short discussion of modal propagation can be found in Thomson and Clilverd (2001).

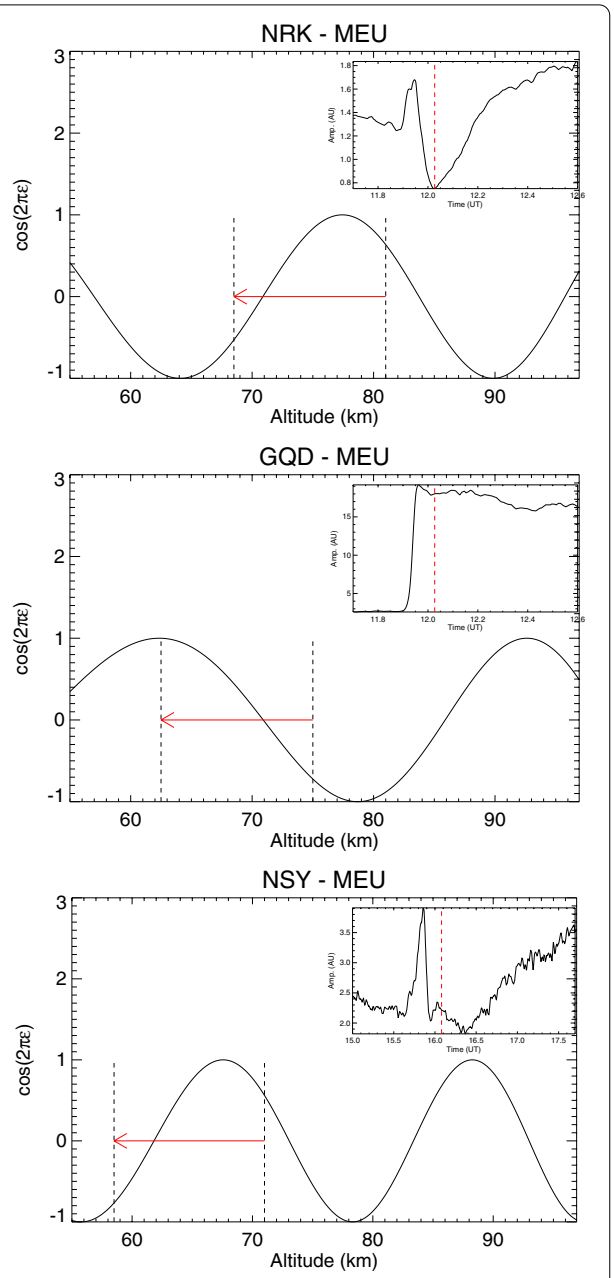

Fig. 3 Interference pattern for NRK (top panel) and GQD (middle panel) and NSY (bottom panel) vs. the reflection height. The sub-panels display the VLF time-profile for the X9.3 flare for NRK and GQD, and the X8.3 for NSY (since the transmitter was off for the biggest flare). Example of reflection height variation during the flare is indicated with the vertical dashed lines, while the arrow indicates the direction followed during the flare rise

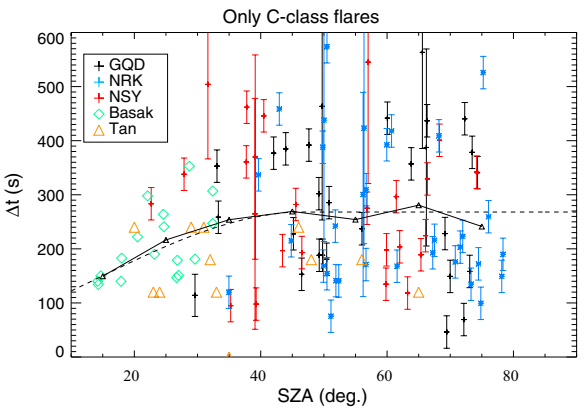

Fig. 4 Time delay as a function of the Solar Zenith Angle. The black triangles represent the average values within bins of 10° and the dashed line is a fit of those points

Analysis

Time delay

Before computing the time delay for all the flares, it is worth discussing its solar zenith angle dependence. Basak and Chakrabarti (2013) concluded that the time delay increases with solar zenith angle. Our measurements extend the values towards larger zenith angles (due to the latitudinal distribution of the transmitters). Following their study, we limit the sampling to C-class flares to avoid trends linked to flare strength (see below). Figure 4 displays our results. The tabulated values of Basak and Chakrabarti (2013) and Tan et al. (2014) (hereafter BCT) have been added for comparison. To estimate the trend, we have defined the average time delay within bins of 10°. They are represented by black triangles and the dashed line is a fit of the data. The time delay increases with solar zenith angle up to about 45° but remains constant above. This constant value serves as reference for the SZA correction of the data. Note however that the correction concerns only about 20% of our sampling.

The time delay is computed for three stations: GQD, NRK, and NSY (Fig. 5). As already noted by the above cited authors and Palit et al. (2015), Δt decreases with increasing flare strength. The new result is the presence of negative time delay for strong flares, i.e. >X2. (Tan et al. 2014; Hayes et al. 2021) also detected some negative time delays, but surprisingly also for flares as weak as C4.4. Figure 2 shows several examples of VLF early response for strong flares. The bottom panel of Fig. 5 displays the results of BCT, with the dashed blue line showing the fit of the data. This fit is reported on the upper panel, which displays our results. The C-class flare are over-represented compared to other class flares. Each class of flare is thus split in nine bins and the average time delay is computed within each bin. Finally, those average points are fitted to define the general trend (in black). Apart from an offset value, the two fits are compatible. In our case, the sign change of Δt occurs around X2 flares, while BCT results would indicate a change around M6.

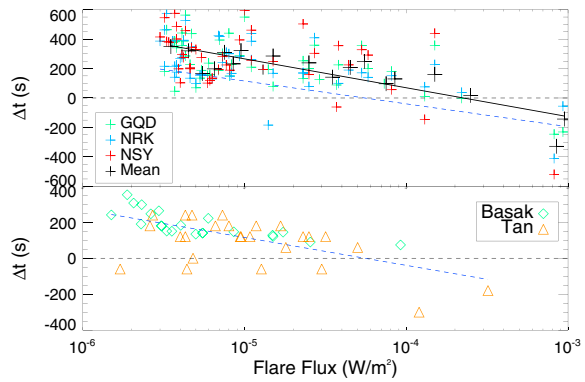

Fig. 5 Δt vs. flare flux from three transmitter (top panel), and results from BCT (bottom panel). On the top panel, the red line displays the fit of our results, the dashed blue curve is the fit of the BCT data (also reproduced on the bottom panel)

The presence of negative Δt is puzzling since it implies that the D-layer maximum ionization is reached before the flare maximum as observed in SXR. This shows that during intense flares another ionization mechanism must precede the SXR radiation and ionize the D-layer. One possible mechanism is the emission of hard X-rays (HXR). In the thick-target model of flare development (Brown 1971), electrons accelerated at the reconnection site in the solar corona are directed downward to the denser chromosphere. Collisional bremsstrahlung from these non-thermal particles generates hard X-rays at the footpoints of the magnetic loops. The heated plasma then evaporates and emits thermal soft X-rays. Thus, HXR are expected to precede SXR by several minutes. In the following, we explore the HXR time and spectral evolution during flares of different classes.

Hard X-ray time and spectral evolution

Ten solar flares were observed both by RHESSI and our VLF antenna. The three strongest flares were selected for a complete analysis through the RHESSI reduction pipeline: the M5.8 of April 3, 2017, the X2.2 of September 6, 2017 and the X8.2 of September 10, 2017. Due to its eclipse orbit, RHESSI missed the main phase of the X9.3.

The time profiles of several RHESSI energy bands for the three selected flares are shown in Fig. 6. For comparison, the time profiles of the two GOES SXR channels (XS and XL) are displayed on the bottom sub-panels. The non-thermal energy range (above 40 keV) gets stronger as the flare strength increases. The emission peak above 40 keV occurs $\approx$ 90 s before the SXR peak (as seen by GOES) for the X2.2, while it reaches up to 7 min earlier for the X8.2. This implies that for M to low X-class flares, considering peak of SXR emission is satisfactory to compute the Δt, since HXR flux is too low or occurs with a time delay comparable to SXR. However, for strong flares like the X8.2, the intense non-thermal component becomes strong enough to start ionizing the ionosphere before the SXR starts playing a role. The VLF identification of the timing of the peak emission occurs now *after* the non-thermal component peak-time (i.e. around 15:58 for the 40 keV range and 16:00 for the VLF emission).

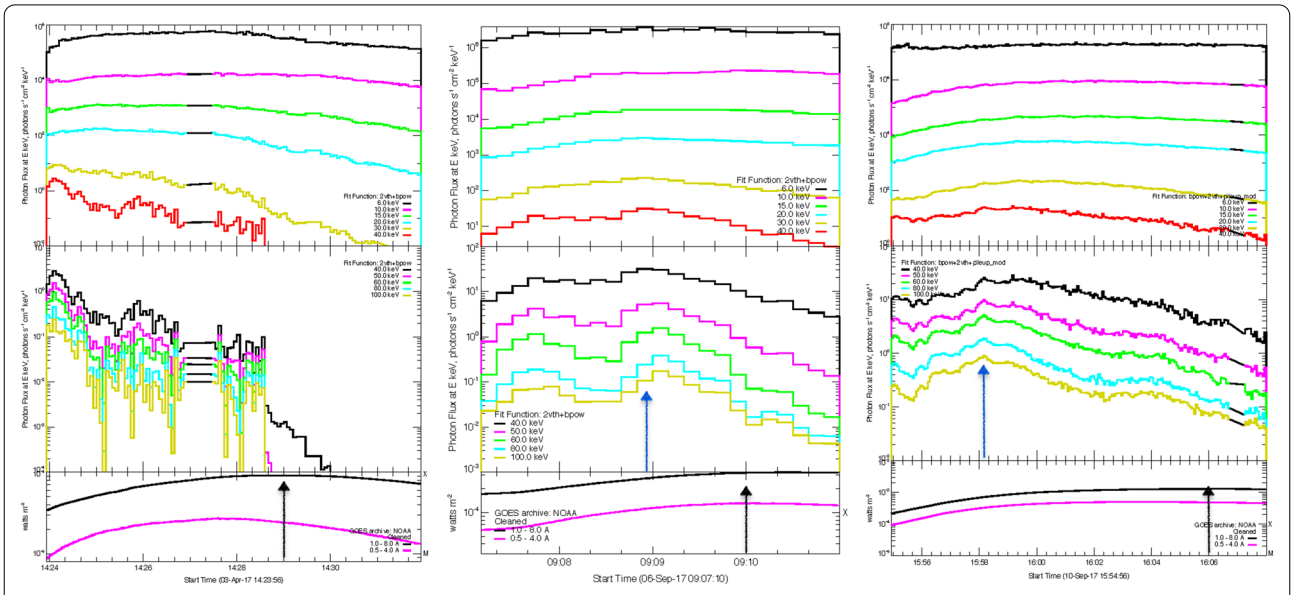

Fig. 6 Time profiles for three flares, M5.8 (April 3, 2017), X2.2 (September 6, 2017) and X8.2 (September 10, 2017) from left to right. For each event, the top and middle panels display RHESSI profiles (respectively, in the energy band 6 to 40 kev and 40 to 100 keV) and the bottom panel displays the two energy bands of GOES. The black arrows indicate the peak time of SXR and the blue arrows the peak time of the 40 keV emission

This means that the time delay remains positive if the peak radiation time is computed from the HXR instead of the SXR.

Figure 7 presents the spectra for the three events at the time of HXR maximum (top panels) and SXR maximum (bottom panel). Following the work of Ning (2009), they are modelized with a bi-thermal component (for the thermal component) and a broken power law (for the non-thermal part of the spectrum). An additional pileup correction is applied for the strong X8.2 flare (the standard pileup correction of the calibration step is conserved for the other events). The higher Chi-square of the X2.2 event results from the poor fitting when the energy reaches the background level above 60 keV. The non-thermal distribution is relatively flat for the M5.8 and X2.2, with an exponent at the HXR peak phase equal to 6.16 and 7.93, respectively. The exponent reaches 3.42 for the X8.2 flare indicating a much harder spectrum. The photon flux is also low or almost equal to the background level for the two first flares, while the X8.2 shows a photon flux about two orders of magnitude above the background at 40 keV. Thus, the non-thermal component, above 40 keV, is probably playing a major role during the strongest flare.

Conclusion

VLF emissions from ground-based transmitters provide powerful measurements to diagnose the ionospheric D-layer. A renewal of interest for this ionospheric layer has grown in the frame of space weather for its role on HF wave propagation and attenuation.

It has long been known that solar flares strongly disturb the ionization rate of the ionosphere. EUV and X-radiation are at the origin of this increase in ionization.

As shown through the analysis of the interference pattern between a ground wave and a single-hop sky wave propagating on short paths between transmitter and receiver stations, the amplitude behaviour of the VLF signal associated with the ionization maximum can be either a peak or a trough. Once this behaviour is understood, the computation of the time delay between the peak of SXR and the perturbation of the VLF signal is possible. The time delay turns negative for the most intense flares, i.e. >X2, which implies that another ionization source is acting on the ionosphere earlier than SXR. Hard X-rays (HXR) have been identified as a possible source. They indeed occur before SXR in most of the flare-development scenarios and produce non-thermal emissions for strong flares. The role of HXR is fundamental in the early stage of the flare only: the SXR remains the most efficient source of ionization after this initial stage.

To evaluate the recombination rate from the computation of the time delay, the contribution of the hard X-rays must be controlled since an error of several minutes in the time delay evaluation can result.

Our analysis is based on a reduced number of events, but the timing analysis is consistent with two other papers that also mentioned negative time delays for flares. Statistical

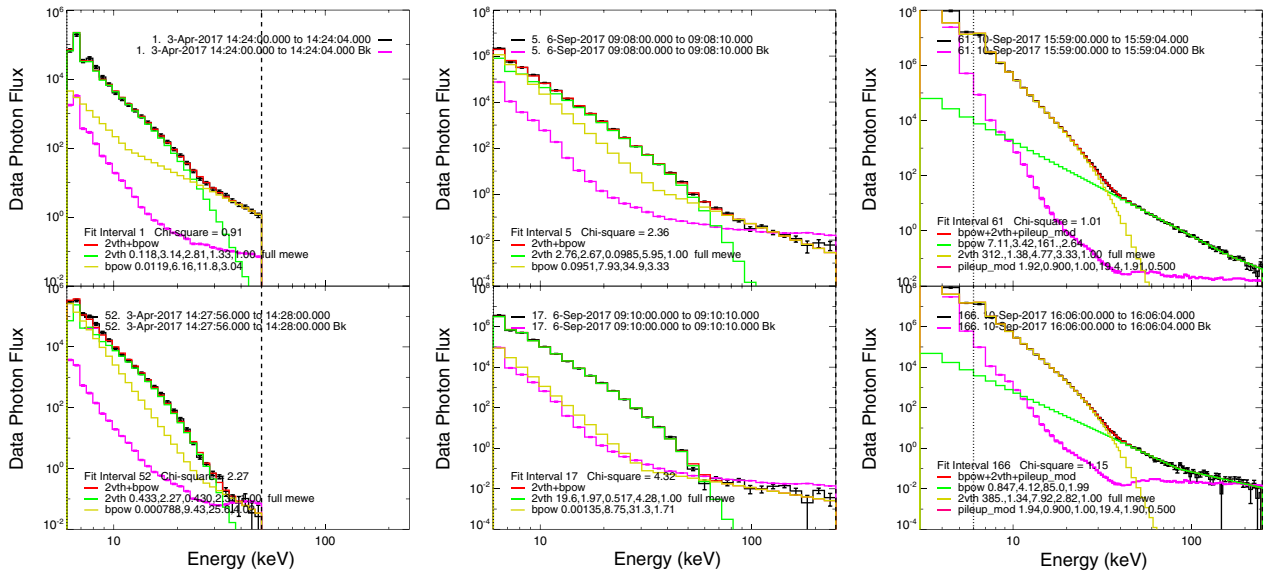

Fig. 7 Photon flux (in photons/s/cm^2) of the flares considered in Fig. 6, for two times: the peak of the HXR (top) and the peak of SXR (bottom). The final black spectrum results from the composition of several fits for the thermal part and non-thermal parts. The model of each fit is described on the bottom left together with the colour code (red, green and yellow). The purple curve indicates the background level. The time interval to build the photon flux is indicated on the upper part of each panel. The vertical dashed line on the left panel indicates the energy limit of the fit

analysis is required to check whether the HXR impact is defined only by the flare strength. The position of the solar active region on the solar surface should not play a critical role since HXR are optically thin radiation.

Appendix A: Flare list

See Table 2.

Table 2 Characteristics of the selected flares

Class	Date (MM/DD/YYYY)	SXR peak flare time [UT]	SZA_{NRK} (deg)	SZA_{GQD} (deg)	SZA_{NSY} (deg)
C6.1	01/21/2017	11:08	79.21	73.08	63.25
C4.1	02/22/2017	13:27	67.51	63.82	58.68
C3.2	03/27/2017	11:12	56.67	50.44	40.55
M5.3	04/02/2017	08:02	73.91	68.30	59.14
M2.3	04/02/2017	13:00	52.05	48.15	43.12
C4.2	04/02/2017	15:08	59.95	60.05	61.46
C3.8	04/03/2017	08:14	71.98	66.22	56.83
C3.9	04/03/2017	11:13	53.85	47.63	37.79
C3.4	04/03/2017	13:06	51.81	48.10	43.45
C7.3	04/03/2017	13:24	52.36	49.21	45.55
M5.8	04/03/2017	14:28	56.09	55.00	54.66
C5.5	04/06/2017	12:10	50.49	45.28	37.72
C3.3	04/18/2017	09:41	56.21	49.73	39.13
C8.0	06/02/2017	17:57	67.23	72.29	80.94
M1.3	07/03/2017	16:14	51.98	55.09	61.24
C4.0	07/09/2017	09:12	50.49	44.62	35.25
C5.3	07/09/2017	12:09	34.97	29.60	22.39
C6.3	08/27/2017	15:16	56.70	57.39	59.83
C7.7	09/02/2017	15:41	61.59	62.89	66.09
C8.3	09/04/2017	12:25	49.93	45.18	38.60
M1.5	09/04/2017	15:30	61.08	62.05	64.77
M3.8	09/05/2017	06:40	82.91	78.56	71.41
C5.4	09/05/2017	10:19	56.35	49.79	39.10
C6.9	09/05/2017	13:34	51.90	49.26	46.51
C3.7	09/05/2017	16:18	67.21	69.44	73.88
C4.6	09/05/2017	17:15	74.47	77.93	84.10
M2.3	09/05/2017	17:43	78.24	82.25	89.18
X2.2	09/06/2017	09:10	63.72	57.37	46.98
X9.3	09/06/2017	12:02	50.94	45.64	37.88
M2.5	09/06/2017	15:56	64.79	66.43	70.04
M1.4	09/07/2017	09:54	59.30	52.74	41.99
X1.1[a]	09/07/2017	10:15	57.34	50.77	40.07
C3.0	09/07/2017	12:14	51.12	46.11	38.96
X1.3	09/07/2017	14:36	56.88	56.22	56.55
M8.1	09/08/2017	07:49	74.40	68.90	59.93
C5.9	09/08/2017	12:13	51.50	46.48	39.28
M2.9	09/08/2017	15:47	64.48	65.85	69.08
M3.7	09/09/2017	11:04	54.35	48.10	38.18
X8.2	09/10/2017	16:06	67.47	69.30	73.13
C3.0	09/12/2017	07:29	78.15	72.86	64.19
C8.1	07/02/2018	13:47	73.29	69.99	65.36
C4.6	10/02/2018	13:22	71.58	67.66	62.00

Table 2 (continued)

Class	Date (MM/DD/YYYY)	SXR peak flare time [UT]	SZA_{NRK} (deg)	SZA_{GQD} (deg)	SZA_{NSY} (deg)
C4.6	03/30/2018	08:04	74.84	69.17	59.91
C5.0	01/26/2019	13:22	76.06	72.15	66.39
M1.1	05/29/2020	07:24	64.37	60.05	53.31
C9.3	05/29/2020	10:46	39.85	33.30	22.67
C3.5	10/16/2020	15:11	75.22	75.11	75.67
C4.3	10/29/2020	11:50	70.79	65.59	57.63
C3.8	11/26/2020	12:53	78.35	74.32	68.30
M4.4	11/29/2020	13:11	79.29	75.62	70.21
C4.0	12/14/2020	14:37	84.82	82.97	80.44
C4.3	04/22/2021	09:21	57.15	50.82	40.49
C3.7	04/22/2021	10:49	48.52	42.05	31.64
C4.0	05/09/2021	13:58	42.94	41.74	41.91
C3.2	05/22/2021	15:35	50.01	52.16	57.00
M1.1	05/22/2021	17:11	62.57	66.82	74.36
M1.1	05/23/2021	11:08	39.09	32.71	22.63
C3.0	05/28/2021	09:57	44.84	38.39	27.87
C3.7	06/09/2021	09:07	49.82	43.96	34.63
C3.6	06/30/2021	18:15	68.21	73.47	82.41
M2.7	07/03/2021	07:17	65.26	61.26	55.07
X1.5	07/03/2021	14:29	39.84	39.91	42.21
M1.0	07/03/2021	17:03	58.52	62.63	70.06
C6.0	07/09/2021	07:55	60.71	56.03	48.72
C7.0	07/09/2021	10:50	39.64	33.08	22.40
C4.7	07/09/2021	17:25	61.89	66.34	74.18
M1.0	10/26/2021	15:57	83.29	84.18	86.11
M1.4	10/28/2021	07:40	89.86	83.76	73.69
M2.0	10/28/2021	10:28	73.57	67.26	57.13
X1.0	10/28/2021	15:35	81.56	81.87	82.94

The three first columns indicate the flare class, the date of occurrence and the peak time as seen in the SXR spectrum. The three last columns indicate the solar zenith angle (SZA) at the reflection point from NSY , GQD, and NRK, respectively.

[a] The GOES flare list indicates an M7.3 while the peak flux of this event is $1.1 \times 10^{-4} W/m^2$. Thus, we label this event as an X1.1

Acknowledgements
The authors thank N. Vilmer for the time spent introducing us to the RHESSI data reduction processes.

Authors' contributions
CB led the project. All authors have participated in the data analysis at a given step of the process. All authors read and approved the final manuscript.

Funding
Not applicable.

Availability of data and materials
The datasets analysed during the current study are available in the following Websites: VLF data: http://sid.stanford.edu/database-browser/. GOES Soft X-Ray data: https://satdat.ngdc.noaa.gov/sem/goes/. RHESSI plots and analysing tools: https://hesperia.gsfc.nasa.gov/rhessidatacenter/spectroscopy.html.

Declarations

Competing interests
The authors declare that they have no competing interests

Author details
[1]LESIA, Observatoire de Paris-PSL, CNRS, Sorbonne Université, Université Paris Cité, Paris, France. [2]British Antarctic Survey, Natural Environment Research Council, Cambridge, UK.

Received: 26 November 2021 Accepted: 23 February 2022
Published online: 15 March 2022

References

Appleton EV (1953) A note on the sluggishness of the ionosphere. J Atmos Terr Phys 3(5):282–284. https://doi.org/10.1016/0021-9169(53)90129-9
Bagiya MS, Thampi SV, Hui D, Sunil AS, Chakrabarty D, Choudhary RK (2018) Signatures of the solar transient disturbances over the low latitude ionosphere during 6 to 8 September 2017. J Geophys Res (Space Phys) 123(9):7598–7608. https://doi.org/10.1029/2018JA025496
Basak T, Chakrabarti SK (2013) Effective recombination coefficient and solar zenith angle effects on low-latitude D-region ionosphere evaluated from VLF signal amplitude and its time delay during X-ray solar flares. Astrophys Space Sci 348:315–326. https://doi.org/10.1007/s10509-013-1597-9

Brown JC (1971) The deduction of energy spectra of non-thermal electrons in flares from the observed dynamic spectra of hard X-ray bursts. Solar Phys 18(3):489–502. https://doi.org/10.1007/BF00149070
Chakraborty S, Ruohoniemi J, Baker J, Nishitani N (2018) Characterization of short-wave fadeout see in daytile SuperDARN ground scatter observations. Radio Sci 43:472–484. https://doi.org/10.1002/1027RS006488
Chakraborty S, Ruohoniemi JM, Baker JBH, Fiori RAD, Bailey SM, Zawdie A (2021) Ionosperic sluggishness: a characteristic time-lag of ionospheric response to solar flares. Space Phys JGR. https://doi.org/10.1029/2020JA028813
Clilverd MA, Thomson NR, Rodger CJ (1999) Sunrise effects on VLF signals propagating over a long north-south path. Radio Sci 34(4):939–948. https://doi.org/10.1029/1999RS900052
De SS, De BK, Pal P, Bandyopadhyay B, Barui S, Haldar DK, Paul S, Sanfui M, Chattopadhyay G (2011) Detection of 2009 leonid, perseid and geminid meteor showers through its effects on transmitted VLF signals. Astrophys Space Sci 332(2):353–357. https://doi.org/10.1007/s10509-010-0513-9
Delcourt J (2003) Ionosphere: region D. Lavoisier, Paris
Dellinger JH (1935) A new cosmic phenomenon. Science 82(2128):351. https://doi.org/10.1126/science.82.2128.351
Deshpande SD, Subrahmanyam CV, Mitra AP (1972) Ionospheric effects of solar flares—I. The statistical relationship between X-ray flares and SID's. J Atmos Terr Phys 34:211–227. https://doi.org/10.1016/0021-9169(72)90165-1
Ellison MA (1950) Ionospheric effects of solar flares. Publ R Obs Edinb 1(4):53–72
Ellison MA (1953) The Hα radiation from solar flares in relation to sudden enhancements of atmospherics on frequencies near 27 Kc/s. J Atmos Terr Phys 4(4):226–239. https://doi.org/10.1016/0021-9169(53)90057-9
Grubor DP, Ulić DMÅ, Žigman V (2008) Classification of X-ray solar flares regarding their effects on the lower ionosphere electron density profile. Ann Geophys 26(7):1731–1740. https://doi.org/10.5194/angeo-26-1731-2008
Haldoupis C, Neubert T, Inan US, Mika A, Allin TH, Marshall RA (2004) Subionospheric early VLF signal perturbations observed in one-to-one association with sprites. J Geophys Res (Space Phys) 109(A18):A10303. https://doi.org/10.1029/2004JA010651
Haldoupis C, Cohen M, Cotts B, Arnone E, Inan U (2012) Long-lasting D-region ionospheric modifications, caused by intense lightning in association with elve and sprite pairs. Geophys Res Lett 39(16):L16801. https://doi.org/10.1029/2012GL052765
Hall JE (1973) Lower ionosphere electron densities from rocket measurements employing LF radio propagation and DC probe techniques. Planet Space Sci 21(1):119–131. https://doi.org/10.1016/0032-0633(73)90024-X
Hayes LA, O'Hara OSD, Murray SA, Gallagher PT (2021) Solar flare effects on the earth's lower ionosphere. Solar Phys 296(11):157. https://doi.org/10.1007/s11207-021-01898-y
Kolarski A, Grubor D (2015) Comparative analysis of VLF signal variation along trajectory induced by X-ray solar flares. J Astrophys Astron 36(4):565–579. https://doi.org/10.1007/s12036-015-9361-x
Křivský L (1962) Flare maximum and the sluggishness of the ionospheric D-region. Bull Astron Inst Czechoslov 13:59
Li W, Yue J, Yang Y, He C, Hu A, Zhang K (2018) Ionospheric and thermospheric responses to the recent strong solar flares on 6 September 2017. J Geophys Res (Space Phys) 123(10):8865–8883. https://doi.org/10.1029/2018JA025700
Lin RP et al (2002) The Reuven Ramaty high-energy solar spectroscopic imager (RHESSI). Solar Phys 210(1):3–32. https://doi.org/10.1023/A:1022428818870
McRae WM, Thomson NR (2004) Solar flare induced ionospheric D-region enhancements from VLF phase and amplitude observations. J Atmos Solar-Terr Phys 66:77–87. https://doi.org/10.1016/j.jastp.2003.09.009
NaitAmor SMA, AlAbdoadaim MB, Cohen BRT, Cotts S, Soula O, Chanrion T, Neubert, Abdelatif T (2010) VLF observations of ionospheric disturbances in association with TLEs from the EuroSprite-2007 campaign. J Geophys Res (Space Phys) 115(1):A00E47. https://doi.org/10.1029/2009JA015026
Ning Z (2009) The investigation of the Neupert effect in two solar flares. Sci China Ser G Phys Mech Astron 52:1686
Palit S, Basak T, Pal S, Chakrabarti SK (2015) Theoretical study of lower ionospheric response to solar flares: sluggishness of D-region and peak time delay. Astrophys Space Sci 356:19–28
Qian L, Wang W, Burns AG, Chamberlin PC, Coster A, Zhang S-R, Solomon SC (2019) Solar flare and geomagnetic storm effects on the thermosphere and ionosphere during 6–11 September 2017. J Geophys Res (Space Phys) 124(3):2298–2311. https://doi.org/10.1029/2018JA026175
Redmon RJ, Seaton DB, Steenburgh R, He J, Rodriguez JV (2018) September 2017's geoeffective space weather and impacts to Caribbean radio communications during hurricane response. Space Weather 16(9):1190–1201. https://doi.org/10.1029/2018SW001897
Rose G, Widdel HU, Azcarraga A, Sanchez L (1972) Experimental evidences for a transient ion layer formation in connection with sudden ionospheric disturbances in the height range 20–50 km. Planet Space Sci 20(6):871–876. https://doi.org/10.1016/0032-0633(72)90172-9
Rozhnoi A, Solovieva M, Fedun V, Gallagher P, McCauley J, Boudjada MY, Shelyag S, Eichelberger HU (2019) Strong influence of solar X-ray flares on low-frequency electromagnetic signals in middle latitudes. Ann Geophys 37:843–850
Scherrer D, Cohen M, Hoeksema T, Inan U, Mitchell R, Scherrer P (2008) Distributing space weather monitoring instruments and educational materials worldwide for IHY 2007: The AWESOME and SID project. Adv Space Res 42(11):1777–1785. https://doi.org/10.1016/j.asr.2007.12.013
Siskind DE, Zawdie KA, Sassi F, Drob D, Friedrich M (2017) Global modeling of the low- and middle-latitude ionospheric D and lower E regions and implications for HF radio wave absorption. Space Weather 15:115–130. https://doi.org/10.1002/2016SW001546
Smith DM et al (2002) The RHESSI spectrometer. Solar Phys 210(1):33–60. https://doi.org/10.1023/A:1022400716414
Tan LM, Thu NN, Ha TQ, Marbouti M (2014) Study of solar flare induced D-region ionosphere changes using VLF amplitude observations at a low latitude site. Indian J Radio Space Phys 43:197–204
Tao C, Nishioka M, Saito S, Shiota D, Watanabe K, Nishizuka N, Tsugawa T, Ishii M (2020) Statistical analysis of short-wave fadeout for extreme space weather event estimation. Earth Planets Space 72(1):173. https://doi.org/10.1186/s40623-020-01278-z
Thomson NR, Clilverd MA (2001) Solar flare induced ionospheric D-region enhancements from VLF amplitude observations. J Atmos Solar-Terr Phys 63(16):1729–1737. https://doi.org/10.1016/S1364-6826(01)00048-7
Thomson NR, Rodger CJ, Clilverd MA (2005), Large solar flares and their ionospheric D region enhancements, *J Geophys Res Space Phys110*
Thomson NR, Clilverd MA, Rodger CJ (2017) Midlatitude ionospheric D region: height, sharpness, and solar zenith angle. J Geophys Res Space Phys 122:8933–8946
Verronen PT, Andersson ME, Marsh DR, Kovács T, Plane JMC (2016) WACCM-D—Whole Atmosphere Community Climate Model with D-region ion chemistry. J Adv Model Earth Syst 8(2):954–975. https://doi.org/10.1002/2015MS000592
Yasyukevich Y, Astafyeva E, Padokhin A, Ivanova V, Syrovatskii S, Podlesnyi A (2018) The 6 September 2017 X-class solar flares and their impacts on the ionosphere, GNSS, and HF radio wave propagation. Space Weather 16(8):1013–1027. https://doi.org/10.1029/2018SW001932
Zigman V, Grubor D, Sulic D (2007) D-region electron density evaluated from VLF amplitude time delay during X-ray solar flares. J Atmos Solar-terr Phys 69:775–792

Publisher's Note